Magnetic Structures and Turbulence in SN 1006 Revealed with Imaging X-Ray Polarimetry

Ping Zhou, Dmitry Prokhorov, Riccardo Ferrazzoli, Yi-Jung Yang, Patrick Slane, Jacco Vink, Stefano Silvestri, Niccolò Bucciantini, Estela Reynoso, David Moffett, et al.

The Astrophysical Journal, 957:55 (12pp), 2023 November 1 https://doi.org/10.3847/1538-4357/acf3e6

Magnetic Structures and Turbulence in SN 1006 Revealed with Imaging X-Ray Polarimetry

Ping Zhou[1], Dmitry Prokhorov[2], Riccardo Ferrazzoli[3], Yi-Jung Yang[4,5], Patrick Slane[6], Jacco Vink[2], Stefano Silvestri[7], Niccolò Bucciantini[8,9,10], Estela Reynoso[11], David Moffett[12], Paolo Soffitta[3], Doug Swartz[13], Philip Kaaret[14], Luca Baldini[7,15], Enrico Costa[3], C.-Y. Ng[4], Dawoon E. Kim[3,16,17], Victor Doroshenko[18], Steven R. Ehlert[14], Jeremy Heyl[19], Frédéric Marin[20], Tsunefumi Mizuno[21], Melissa Pesce-Rollins[7], Carmelo Sgrò[7], Toru Tamagawa[22], Martin C. Weisskopf[14], Fei Xie[3,23], Iván Agudo[24], Lucio A. Antonelli[25,26], Matteo Bachetti[27], Wayne H. Baumgartner[14], Ronaldo Bellazzini[7], Stefano Bianchi[28], Stephen D. Bongiorno[14], Raffaella Bonino[29,30], Alessandro Brez[7], Fiamma Capitanio[3], Simone Castellano[7], Elisabetta Cavazzuti[31], Chien-Ting Chen[13], Stefano Ciprini[17,26], Alessandra De Rosa[3], Ettore Del Monte[3], Laura Di Gesu[31], Niccolò Di Lalla[32], Alessandro Di Marco[3], Immacolata Donnarumma[31], Michal Dovčiak[33], Teruaki Enoto[22], Yuri Evangelista[3], Sergio Fabiani[3], Javier A. Garcia[34], Shuichi Gunji[35], Kiyoshi Hayashida[36], Wataru Iwakiri[37], Svetlana G. Jorstad[38,39], Fabian Kislat[40], Vladimir Karas[33], Takao Kitaguchi[22], Jeffery J. Kolodziejczak[14], Henric Krawczynski[41], Fabio La Monaca[3], Luca Latronico[29], Ioannis Liodakis[42], Simone Maldera[29], Alberto Manfreda[43], Andrea Marinucci[31], Alan P. Marscher[38], Herman L. Marshall[44], Giorgio Matt[28], Ikuyuki Mitsuishi[45], Fabio Muleri[3], Michela Negro[46,47,48], Stephen L. O'Dell[14], Nicola Omodei[32], Chiara Oppedisano[29], Alessandro Papitto[25], George G. Pavlov[49], Abel L. Peirson[32], Matteo Perri[25,26], Pierre-Olivier Petrucci[50], Maura Pilia[27], Andrea Possenti[27], Juri Poutanen[51], Simonetta Puccetti[26], Brian D. Ramsey[14], John Rankin[3], Ajay Ratheesh[3], Oliver Roberts[13], Roger W. Romani[32], Gloria Spandre[7], Fabrizio Tavecchio[52], Roberto Taverna[53], Yuzuru Tawara[45], Allyn F. Tennant[14], Nicholas E. Thomas[14], Francesco Tombesi[17,54,55], Alessio Trois[27], Sergey S. Tsygankov[51], Roberto Turolla[53,56], Kinwah Wu[56], and Silvia Zane[56]

[1] School of Astronomy and Space Science, Nanjing University, Nanjing 210023, People's Republic of China; pingzhou@nju.edu.cn
[2] Anton Pannekoek Institute for Astronomy & GRAPPA, University of Amsterdam, Science Park 904, 1098 XH Amsterdam, The Netherlands
[3] INAF Istituto di Astrofisica e Planetologia Spaziali, Via del Fosso del Cavaliere 100, I-00133 Roma, Italy
[4] Department of Physics, The University of Hong Kong, Pokfulam, Hong Kong, People's Republic of China
[5] Laboratory for Space Research, The University of Hong Kong, Hong Kong, People's Republic of China
[6] Center for Astrophysics Harvard & Smithsonian, 60 Garden Street, Cambridge, MA 02138, USA
[7] Istituto Nazionale di Fisica Nucleare, Sezione di Pisa, Largo B. Pontecorvo 3, I-56127 Pisa, Italy
[8] INAF Osservatorio Astrofisico di Arcetri, Largo Enrico Fermi 5, I-50125 Firenze, Italy
[9] Dipartimento di Fisica e Astronomia, Università degli Studi di Firenze, Via Sansone 1, I-50019 Sesto Fiorentino (FI), Italy
[10] Istituto Nazionale di Fisica Nucleare, Sezione di Firenze, Via Sansone 1, I-50019 Sesto Fiorentino (FI), Italy
[11] Instituto de Astronomía y Física del Espacio (IAFE), Av. Int. Guiraldes 2620, Pabellón IAFE, Ciudad Universitaria, 1428 Ciudad Autónoma de Buenos Aires, Argentina
[12] Department of Physics, Furman University, Greenville, SC 29613, USA
[13] Science and Technology Institute, Universities Space Research Association, Huntsville, AL 35805, USA
[14] NASA Marshall Space Flight Center, Huntsville, AL 35812, USA
[15] Dipartimento di Fisica, Università di Pisa, Largo B. Pontecorvo 3, I-56127 Pisa, Italy
[16] Dipartimento di Fisica, Università degli Studi di Roma "La Sapienza," Piazzale Aldo Moro 5, I-00185 Roma, Italy
[17] Istituto Nazionale di Fisica Nucleare, Sezione di Roma "Tor Vergata," Via della Ricerca Scientifica 1, I-00133 Roma, Italy
[18] Institut für Astronomie und Astrophysik, Universität Tübingen, Sand 1, D-72076 Tübingen, Germany
[19] University of British Columbia, Vancouver, BC V6T 1Z4, Canada
[20] Université de Strasbourg, CNRS, Observatoire Astronomique de Strasbourg, UMR 7550, F-67000 Strasbourg, France
[21] Hiroshima Astrophysical Science Center, Hiroshima University, 1-3-1 Kagamiyama, Higashi-Hiroshima, Hiroshima 739-8526, Japan
[22] RIKEN Cluster for Pioneering Research, 2-1 Hirosawa, Wako, Saitama 351-0198, Japan
[23] Guangxi Key Laboratory for Relativistic Astrophysics, School of Physical Science and Technology, Guangxi University, Nanning 530004, People's Republic of China
[24] Instituto de Astrofísica de AndalucíaCSIC, Glorieta de la Astronomía s/n, E-18008 Granada, Spain
[25] INAF Osservatorio Astronomico di Roma, Via Frascati 33, I-00078 Monte Porzio Catone (RM), Italy
[26] Space Science Data Center, Agenzia Spaziale Italiana, Via del Politecnico snc, I-00133 Roma, Italy
[27] INAF Osservatorio Astronomico di Cagliari, Via della Scienza 5, I-09047 Selargius (CA), Italy
[28] Dipartimento di Matematica e Fisica, Università degli Studi Roma Tre, Via della Vasca Navale 84, I-00146 Roma, Italy
[29] Istituto Nazionale di Fisica Nucleare, Sezione di Torino, Via Pietro Giuria 1, I-10125 Torino, Italy
[30] Dipartimento di Fisica, Università degli Studi di Torino, Via Pietro Giuria 1, I-10125 Torino, Italy
[31] ASI—Agenzia Spaziale Italiana, Via del Politecnico snc, I-00133 Roma, Italy
[32] Department of Physics and Kavli Institute for Particle Astrophysics and Cosmology, Stanford University, Stanford, CA 94305, USA
[33] Astronomical Institute of the Czech Academy of Sciences, Boční II 1401/1, 14100 Praha 4, Czech Republic
[34] California Institute of Technology, Pasadena, CA 91125, USA
[35] Yamagata University,1-4-12 Kojirakawa-machi, Yamagata-shi 990-8560, Japan
[36] Osaka University, 1-1 Yamadaoka, Suita, Osaka 565-0871, Japan
[37] International Center for Hadron Astrophysics, Chiba University, Chiba 263-8522, Japan
[38] Institute for Astrophysical Research, Boston University, 725 Commonwealth Avenue, Boston, MA 02215, USA
[39] Department of Astrophysics, St. Petersburg State University, Universitetsky pr. 28, Petrodvoretz, 198504 St. Petersburg, Russia
[40] Department of Physics and Astronomy and Space Science Center, University of New Hampshire, Durham, NH 03824, USA
[41] Physics Department and McDonnell Center for the Space Sciences, Washington University in St. Louis, St. Louis, MO 63130, USA
[42] Finnish Centre for Astronomy with ESO, 20014 University of Turku, Finland

[43] Istituto Nazionale di Fisica Nucleare, Sezione di Napoli, Strada Comunale Cinthia, I-80126 Napoli, Italy
[44] MIT Kavli Institute for Astrophysics and Space Research, Massachusetts Institute of Technology, 77 Massachusetts Avenue, Cambridge, MA 02139, USA
[45] Graduate School of Science, Division of Particle and Astrophysical Science, Nagoya University, Furo-cho, Chikusa-ku, Nagoya, Aichi 464-8602, Japan
[46] University of Maryland, Baltimore County, Baltimore, MD 21250, USA
[47] NASA Goddard Space Flight Center, Greenbelt, MD 20771, USA
[48] Center for Research and Exploration in Space Science and Technology, NASA/GSFC, Greenbelt, MD 20771, USA
[49] Department of Astronomy and Astrophysics, Pennsylvania State University, University Park, PA 16802, USA
[50] Université Grenoble Alpes, CNRS, IPAG, F-38000 Grenoble, France
[51] Department of Physics and Astronomy, 20014 University of Turku, Finland
[52] INAF Osservatorio Astronomico di Brera, Via E. Bianchi 46, I-23807 Merate (LC), Italy
[53] Dipartimento di Fisica e Astronomia, Università degli Studi di Padova, Via Marzolo 8, I-35131 Padova, Italy
[54] Dipartimento di Fisica, Università degli Studi di Roma "Tor Vergata," Via della Ricerca Scientifica 1, I-00133 Roma, Italy
[55] Department of Astronomy, University of Maryland, College Park, MD 20742, USA
[56] Mullard Space Science Laboratory, University College London, Holmbury St Mary, Dorking, Surrey RH5 6NT, UK
Received 2023 July 28; revised 2023 August 22; accepted 2023 August 23; published 2023 October 27

Abstract

Young supernova remnants strongly modify the surrounding magnetic fields, which in turn play an essential role in accelerating cosmic rays (CRs). The X-ray polarization measurements probe magnetic field morphology and turbulence at the immediate acceleration site. We report the X-ray polarization distribution in the northeastern shell of SN 1006 from a 1 Ms observation with the Imaging X-ray Polarimetry Explorer. We found an average polarization degree of $22.4\% \pm 3.5\%$ and an average polarization angle of $-45\overset{\circ}{.}4 \pm 4\overset{\circ}{.}5$ (measured on the plane of the sky from north to east). The X-ray polarization angle distribution reveals that the magnetic fields immediately behind the shock in the northeastern shell of SN 1006 are nearly parallel to the shock normal or radially distributed, similar to that in the radio observations, and consistent with the quasi-parallel CR acceleration scenario. The X-ray emission is marginally more polarized than that in the radio band. The X-ray polarization degree of SN 1006 is much larger than that in Cas A and Tycho, together with the relatively tenuous and smooth ambient medium of the remnant, favoring that CR-induced instabilities set the magnetic turbulence in SN 1006, and CR acceleration is environment-dependent.

Unified Astronomy Thesaurus concepts: Supernova remnants (1667); Polarimetry (1278); X-ray astronomy (1810); Shocks (2086); Cosmic rays (329)

1. Introduction

Supernova remnants (SNRs) are regarded as factories of relativistic particles. Baade & Zwicky (1934) first proposed supernovae as a potential origin of cosmic rays (CRs) in the 1930s. The first observational evidence for their hypothesis was the detection of radio emission from SNRs. The radio emission is found to be nonthermal, generated by the relativistic electrons gyrating in the magnetic fields (e.g., van der Laan 1962). Nevertheless, it lacked direct evidence for SNRs accelerating CRs up to energies of 100 TeV until the discovery of nonthermal X-ray emission from the bilateral shells of SN 1006 (Koyama et al. 1995). In the high-energy regime, H.E.S.S. and Fermi-LAT observations show that SN 1006 has a shell-like morphology in the TeV and GeV bands (Acero et al. 2010; Xing et al. 2016; Condon et al. 2017), further confirming the particle acceleration in the shock front. In addition, X-ray synchrotron emission has been detected in a few other young SNRs that drive fast shocks with speeds of a few thousand kilometers per second. As synchrotron emission is produced by relativistic electrons gyrating in the magnetic fields, it keeps crucial information on particle acceleration, radiative processes, and magnetic fields.

Two key questions in the study of CRs are how magnetic fields influence CR acceleration and how SNRs and their CRs modify magnetic fields. The diffusive shock acceleration theory has predicted that magnetic fields can be strongly amplified through either the streaming instability (Bell 2004) or turbulent dynamo progress via density fluctuations (e.g., Giacalone & Jokipii 2007). This prediction is supported by the presence of thin X-ray synchrotron filaments and rapid variability of nonthermal X-ray spots in young SNRs, where the magnetic fields are found to be orders of magnitude stronger than the typical value in the Galaxy (Vink & Laming 2003; Parizot et al. 2006; Uchiyama et al. 2007). The X-ray observations before the launch of the Imaging X-ray Polarimetry Explorer (IXPE) had not directly revealed how the amplified magnetic fields are orientated and ordered. Magnetic field amplification and turbulence are suggested to occur close to the shock fronts, which are best traced by the X-ray synchrotron emission. Thus, X-ray polarization measurements directly probe the magnetic field direction and turbulence, helping with the understanding of the mechanisms of magnetic field amplification. The X-ray polarization angle (PA; measured on the plane of the sky from north to east; International Astronomical Union standard) orients perpendicularly to the magnetic fields, while the polarization degree (PD) reflects the turbulence level, with more ordered magnetic fields probed with a high PD.

IXPE (Weisskopf et al. 2022) opened the imaging X-ray polarization window to probe magnetic field distribution and turbulence in high-energy sources, including SNRs. The very recent X-ray polarization measurements of the young SNRs Cas A (Vink et al. 2022b) and Tycho (Ferrazzoli et al. 2023) showed radially distributed magnetic fields. Cas A has a relatively low PD of ~5% at the outer rim, while Tycho is more polarized, with a PD of ~12%. The difference in PD suggests a different turbulence level or scale between these two SNRs, but both are smaller than the theoretical maximum value

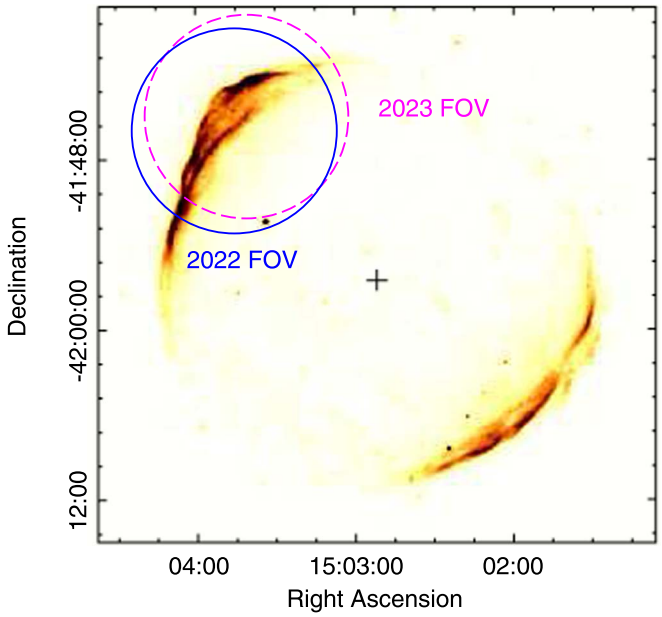

Figure 1. Field of view of the two IXPE observations overlaid on the XMM-Newton 2–8 keV image of SN 1006 (Li et al. 2016). The plus sign denotes the SNR center ($15^h02^m51\overset{s}{.}7$, $-41°56'33''$, J2000) located by Reynolds & Gilmore (1986) and Winkler & Long (1997).

of PD $_{\max} = \Gamma/(\Gamma + 2/3) \sim 80\%$, where Γ is the photon index.

SN 1006 (G327.6+14.6) was the third SNR observed with IXPE. It is a Galactic SNR with a diameter of $\sim 0\overset{\circ}{.}5$ at a distance of 2.18 ± 0.08 kpc (Winkler et al. 2003). The IXPE observation covered the SNR's northeastern shell, which is composed of two rims (see circles in Figure 1). This remnant has some unique properties for studying magnetic turbulence and CR acceleration. First, SN 1006 is among the best sources for probing spatially resolved magnetic properties, since its nonthermal rims with typical widths of $\sim 20''$–$30''$ (Bamba et al. 2004; Ressler et al. 2014) can be roughly resolved by IXPE with an angular resolution of $\sim 30''$ (Weisskopf et al. 2022). The bright nonthermal rims are produced by TeV electrons in magnetic fields amplified to tens of the Galactic level (Parizot et al. 2006) and are not contaminated by thermal emission in 2–8 keV. Second, SN 1006 evolves in a tenuous ambient medium high above the Galactic plane ($\sim$560 pc), in contrast to Cas A and Tycho, which are both located in the Galactic plane. The density fluctuation of the northeastern and eastern shells appears small, explaining the faint and fairly uniform surface brightness of the H_α emission (Winkler et al. 2003; Giuffrida et al. 2022). Thus, SN 1006 is a test bed to study magnetic turbulence driven predominately by CRs because the turbulence from small-scale density fluctuations is not considered an essential factor in this remnant. Third, the bilateral morphology of SN 1006 in both the X-ray (Koyama et al. 1995) and radio (Reynolds & Gilmore 1986) bands has been attributed to the magnetic field orientation (Fulbright & Reynolds 1990; Petruk et al. 2009; West et al. 2016). SN 1006 has been the target of observations for a long-standing question on whether magnetic fields "quasi-parallel" or "quasi-perpendicular" to shocks are more efficient in accelerating particles (Bamba et al. 2004; Reynoso et al. 2013; Winkler et al. 2014). In particular, Rothenflug et al. (2004) suggested that the bright X-ray synchrotron is associated with the polar caps, suggesting that the magnetic field runs parallel to the shock normal. A direct way to answer the question is to measure the magnetic field distribution and turbulence in SN 1006.

2. Observations and Data Reduction

2.1. IXPE

IXPE works in the 2–8 keV band (Weisskopf et al. 2022). It contains three X-ray telescopes. A detector unit (DU) is placed at the focus of each telescope, and each contains a gas-pixel detector (Costa et al. 2001; Bellazzini et al. 2006) that probes the polarization of X-ray photons. IXPE provides an angular resolution of $24''$–$30''$ (half-power diameter), a total effective area of ~ 76 cm^2 at 2.3 keV, and a field of view of $12\overset{'}{.}9$ in diameter (Weisskopf et al. 2022), which allow for imaging polarimetry of extended sources such as SNRs.

IXPE observed the northeastern shell of SN 1006 (see Figure 1) on 2022 August 5–19 with ID 01006801 and 2023 March 3–10 with ID 02001701. The live time of the three detectors is 628–641 ks for the observation in 2022 and 339 ks in 2023. A small fraction of observations suffered from the contamination of solar flares, which caused high photon flux in the light curves of the data. To assess that, we binned the 2–8 keV photons from the source region (northeastern shell) every 120 s and obtained the light curves. To remove the time with solar flare contamination, we used a Gaussian function to fit the count rate distribution and filtered out the time intervals showing count rates higher than 3σ above the mean level. Consequently, 3–5 ks were removed in 2022 and 2–3 ks in 2023 for DU1–3.

The software *ixpeobssim* (vers. 30.0; Baldini et al. 2022) was applied to reduce and analyze the IXPE data. We used version 12 of the *ixpeobssim* instrument response functions of the HEASARC CALDB. The algorithm PMAPCUBE in *xpbin* under the *ixpeobssim* software is applied to produce images of Stokes *I*, *Q*, and *U*; PD; and PA. A few regions of interest are selected for in-depth analysis. Further polarization analysis for binned (e.g., within given regions) data products used the PCUBE algorithm in *xpbin*. We extracted spectra of Stokes *I*, *Q*, and *U* with the PHA1, PHAQ1, and PHAU1 algorithms in *xpbin*, respectively. In the spectropolarimetric analysis, we used weighted analysis and the weight response files (Di Marco et al. 2022). The Stokes *I* spectra were grouped to reach at least 50 counts bin^{-1}. A constant 0.4 keV energy binning is applied to the Stokes *Q* and *U* spectra. The spectra were analyzed using the Xspec package (vers. 12.12.1) in the HEASoft software.

In the polarimetric analysis, we did not correct the vignetting effect. The vignetting does not influence the instrumental background. The emission crossing the mirror module assemblies is affected, but the Stokes parameters *I*, *Q*, and *U* are subject to the vignetting in the same way; thus, the source PD and PA are not much influenced: $\mathrm{PD} = \sqrt{Q^2 + U^2}/I$, $Q/I = \cos(2\mathrm{PA})$, and $U/I = \sin(2\mathrm{PA})$. Nevertheless, for large regions covering on- and off-axis positions, vignetting puts more weight on the on-axis position, where the effective area is larger.

2.2. Other Data

We retrieved the XMM-Newton EPIC data of SN 1006 taken in 2009 (ObsID: 0555630301; PI: A. Decourchelle) with a total exposure of 125 ks. After filtering out the intervals with heavy proton flares, the net exposure is 87/89/60 ks for the MOS1/MOS2/pn camera. The data reduction was conducted using the

Science Analysis System software (vers. 19.1; SAS Development Team 2014), and the spectra were analyzed using Xspec.

For comparison purposes, we also used the 1.4 GHz radio polarization data of SN 1006 (Reynoso et al. 2013) taken with the Australia Telescope Compact Array. We used the Stokes *I*, *Q*, and *U* radio images to calculate the degree and angle of polarization (PD_r and PA_r) in a few regions of interest, which will be elaborated in Section 4.4. The polarized radio emission suffered from Faraday rotation in the ionized foreground medium, which causes a rotation of the PA with the square of the wavelength λ^2: $PA_r^{obs} = PA_r + RM\,(\lambda/1\,m)^2$. Following Reynoso et al. (2013), a uniform rotation measure (RM) of $12\,rad\,m^{-2}$ is applied in this work to obtain the original PA PA_r, although there could be local variations of the RM in the SNR.

2.3. Position Correction of the IXPE Data

There was an offset of the IXPE pointing in the two epochs of observations for SN 1006. A misalignment was also found in the Cas A observations with the order of 2.′5 (Vink et al. 2022b) and in one of the Tycho SNR observations (Ferrazzoli et al. 2023). The focal pointing (*x*, *y*) has an offset due to the boom bending and the difficulty of the bending correction for extended sources (Weisskopf et al. 2022). We did not consider the rotation angle correction, as it is small compared to the angular resolution of IXPE. The roll angle of IXPE is determined to an accuracy of 0.°7. Across the field of view with a diameter of 12.′9, the maximum shift in the position of an X-ray source due to roll angle error is 4.″7.

To correct for the positions of the two-epoch IXPE observations, we simulated a reference image using the XMM-Newton X-ray image of SN 1006 taken in 2009 (ObsID: 0555630301; PI: A. Decourchelle). We are aware that the SNR shell has a proper motion of $\sim$0.″48 yr^{-1} (Katsuda et al. 2009), which can cause a northeastern motion of $\sim$6″ for the shell in a baseline of 13 yr. Nevertheless, given the angular resolution of 30″ for IXPE, such a small offset does not significantly influence our polarization studies. From the XMM-Newton 2–8 keV image and spectrum, we simulated a 10 Ms IXPE observation with *ixpeobssim* and obtained the reference image with a pixel size of 2.″46. Then we compared the reference image, *img*1, and the observed image, *img*2 (also binned with a pixel size of 2.″46), with an offset (*dx*, *dy*) added. The best-fit offset (*dx*, *dy*) is obtained when the deviation between the two images $\sum_{i=1}^{n}[img2(i) - img1(i)]^2$ reaches the minimum, where *i* and *n* are the *i*th pixel and pixel number, respectively. With this algorithm, we estimate offsets of (−14.″8, 0″) for the observation in 2022 and (49.″3, 24.″6) for the observation in 2023, but the offset correction could have an uncertainty. Based on a visual check, the final offset is much smaller than the angular resolution of IXPE.

2.4. Background Analysis

The background analysis is crucial for faint or extended sources observed with IXPE (Xie et al. 2021; Di Marco et al. 2023; Ferrazzoli et al. 2023). Among the three SNRs observed so far by IXPE, SN 1006 is the faintest; thus, the background contribution needs to be considered. The background photons have two contributions: the diffuse X-ray background near SN 1006 and the particle-induced instrumental background, which is nearly uniform across the detector. Since SN 1006 is located at a high Galactic latitude ($b = 14.°6$), the Galactic diffuse background is small. The 2–8 keV background level of previous IXPE observations was found to be in the range of 8.7–12.1 $\times 10^{-4}$ counts s^{-1} $arcmin^{-2}$ (Di Marco et al. 2023). We conducted an energy-dependent background rejection by selecting the events with the event-track region of interest following the strategy by Di Marco et al. (2023). This removes up to 40% of the instrumental background events.

The residual background is still nonnegligible, so we selected a source-free region outside SN 1006 to estimate the background. Emission in this region includes the local (sky) background of SN 1006 and the residual instrumental background. We obtained a background level of 5.1–5.9 $\times 10^{-4}$ counts s^{-1} $arcmin^{-2}$ in 2–8 keV in DU1–3, while at the SNR shell, we obtained 1.9–2.0 $\times 10^{-3}$ counts s^{-1} $arcmin^{-2}$. Therefore, the background contributes $\sim$30% of the photons from the shell region.

3. Results

3.1. Polarization Images

IXPE allows a spatially resolved polarization study of the double-rim structure in the northeastern shell of SN 1006. Figure 2 (left) shows the Stokes *I* count morphology in the 2–4 keV band with a pixel size of 10″. We selected the 2–4 keV energy band to minimize the contamination from the strong instrumental background above 4 keV (see the Appendix and Figure 5). The distribution of polarized X-ray emission in the northeast of SN 1006 with a bin size of 1.′5 is also shown in Figure 2 (right). The polarized emission is made using the Stokes *Q* and *U* maps ($\sqrt{Q^2 + U^2}$) and generally follows the distribution of Stokes *I*.

The PD distribution in the shell is shown in the lower left panel of Figure 2 (pixel size of 1.′5). The magnetic vectors and 1σ uncertainty range are overlaid on pixels with a pretrial confidence level of $CL_{pre} > 95\%$ (2σ). In these pixels, the PDs range from 14% to 25%, and the uncertainty is $\approx$6%, except for the southern pixel with a larger error of 9%.The PA values for most of these pixels are around −45° with an error of 8°–11°, except for the southern pixel with PA = −3°. The overall magnetic orientation tends to be parallel to the shock normal, consistent with the radio polarization measurement (Reynoso et al. 2013).

The quoted significance level per pixel is the pretrial significance, not corrected for the number of pixels. Each independent pixel contributes to a trial, and as the number of trials (pixels) increases, the probability of finding a "significant" random fluctuation also increases. In the shell with $N = 23$ independent pixels, the probability of finding no random deviation above a significance threshold (here taking CL_{pre}) is $CL_{post} = CL_{pre}{}^{N}$. Assuming a uniform PD error across the shell, we obtained the posttrial confidence level distribution as shown in the lower right panel of Figure 2. The most significant pixel in the shell has $CL_{post} = 97\%$, and 2 more pixels show $CL_{post} = 87\%$–88%. To increase the significance, we need to enlarge the pixel size or select larger regions. Moreover, the PD values are not corrected for the background, which introduces unpolarized photons that may reduce the PD values.

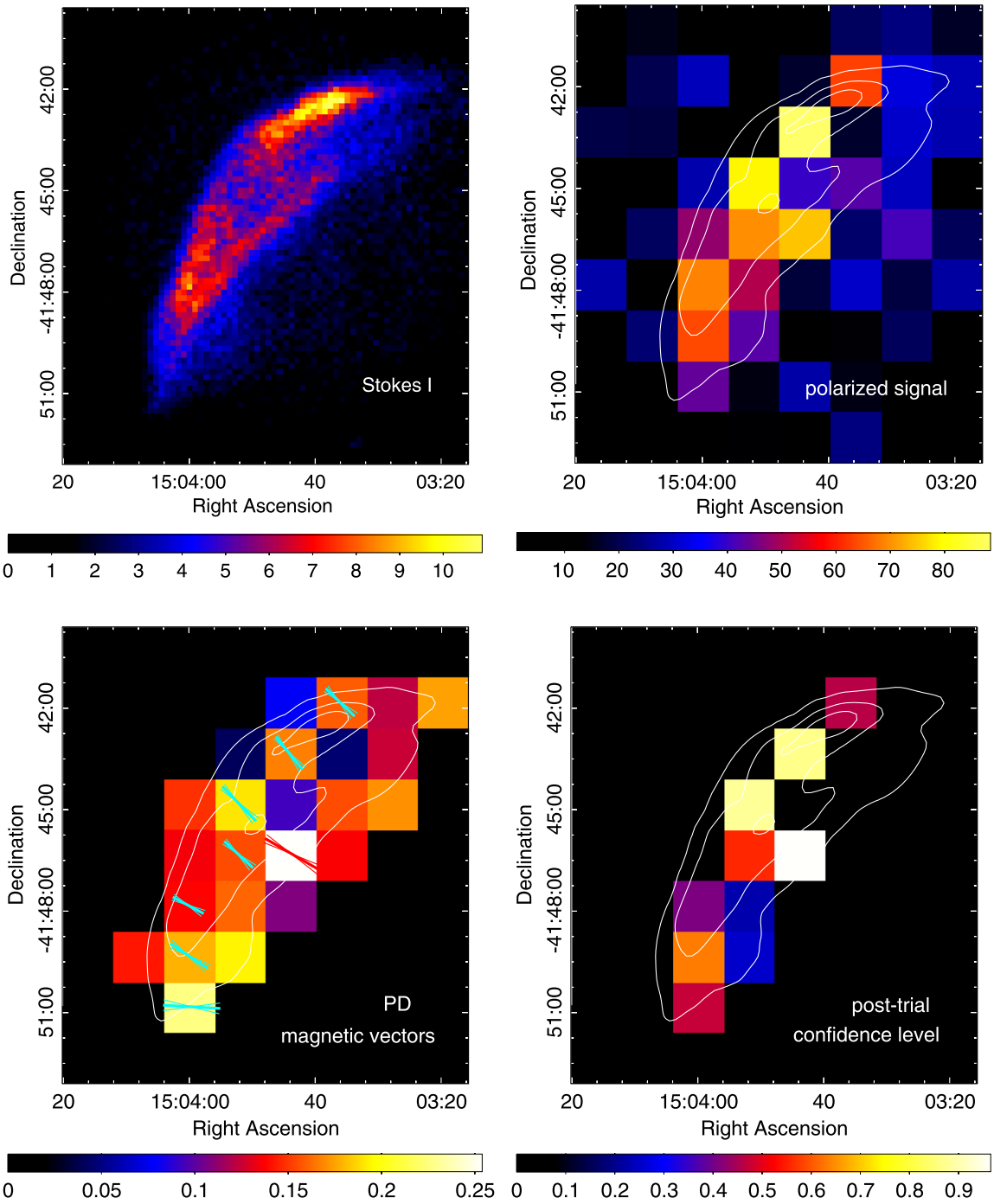

Figure 2. IXPE images of the northeastern shell of SN 1006 in the 2–4 keV band. Upper left: Stokes I image with a pixel size of 10″. Upper right: polarized signal ($\sqrt{Q^2 + U^2}$; right) image binned with a pixel size of 1.′5. Lower left: PD distribution for pixels with Stokes I >158 counts (to mask out pixels with low X-ray brightness), overlaid with magnetic vectors and their 1σ errors. The blue and red vectors correspond to pixels with a pretrial significance of 2σ–3σ and >3σ, respectively. The length of the magnetic vectors scales with the polarized degree. Lower right: the posttrial confidence level for the detection of the polarized signal. The white contours show the Stokes I levels.

3.2. Polarization Properties of Regions

To accurately measure the polarization parameters for SN 1006, we need to consider the contribution of background photons in the source regions. We calculated the polarization parameters of five regions by taking the background from a nearby source-free region (see the dashed regions in Figure 3). The regions include "Shell" for the whole northeastern shell of SN1006, regions A and B for the outer filaments, and regions C and D for the inner filament (see Figure 3). This region division allows for studying polarization differences between filaments and investigating PA variation with the position angle of the structures relative to the SNR center.

The PDs and PAs with their 50%, 90%, 99%, and 99.9% confidence level contours of the five regions are shown as polar plots in Figure 3, and the values are tabulated in Table 1. The polarization signal from the whole northeastern shell is detected at a significance of 6.3σ, while the four regions A–D are

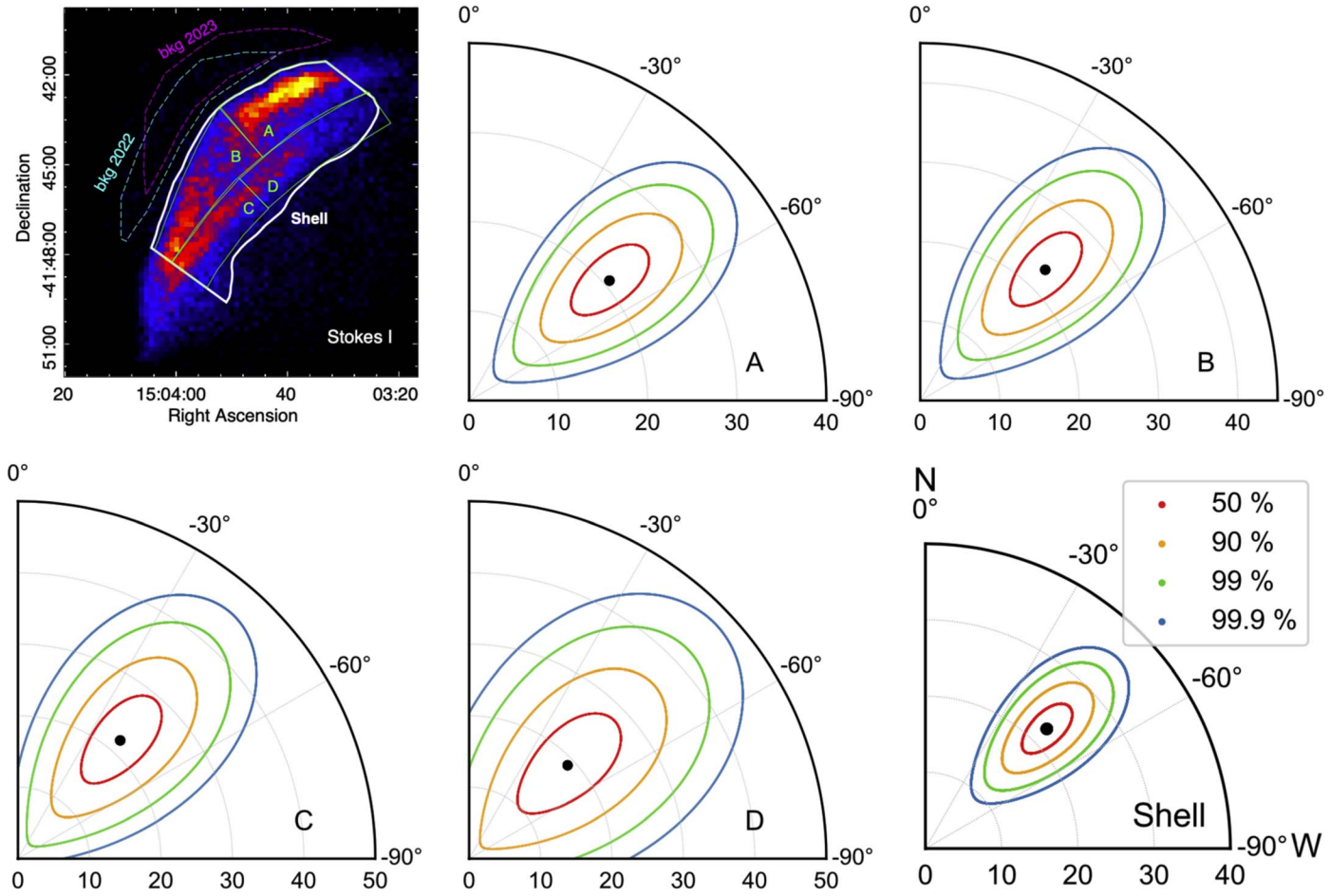

Figure 3. Stokes *I* image with regions and the polar plots of these regions in the 2–4 keV band. In the first panel, the regions delineated with solid and dashed lines correspond to the source and background regions, respectively. Each polar plot shows the PD (%) and PA in radial and position angle coordinates, respectively, with the background subtracted. The best-fit PD and PA values are denoted by black dots. The 50%, 90%, 99%, and 99.9% confidence levels (based upon χ^2 on two degrees of freedom) are coded in red, orange, green, and blue, respectively.

detected at the 2.5σ–4.6σ level. The average polarization of the northeastern shell is $22.4\% \pm 3.5\%$, and the PA is $-45\overset{\circ}{.}4 \pm 4\overset{\circ}{.}5$. Three smaller regions show a PD of 21%–23% and PAs between -50° and -40°, consistent with those of the entire shell. The outer filaments (A and B) and the inner filament (C and D) reveal identical PDs, implying a similar turbulence level of the magnetic fields. The PAs in the southern (B and C) and northern (A and D) regions cannot be distinguished considering the error range.

Different methods exist to divide the northeastern shell and select regions. We also selected regions based on X-ray brightness distribution, as elaborated in the Appendix. We found that the PD is nearly uniform (PD $\sim$ 20%–26%) and does not show a correlation with the X-ray brightness.

Previous radio polarization measurements of SN 1006 found that the magnetic fields are predominantly radially distributed but also contain components nearly parallel to the Galactic plane (Reynoso et al. 2013). To test whether the IXPE measurements support a radial magnetic geometry, we reconstruct events files based on the circular polarization geometry model using the *xpstokesalign* command in *ixpeobssim* and check whether this approach improves the detection of polarization. The initial Stokes parameters q_k and u_k of each event are rotated with respect to the SNR center at R.A. (J2000) $= 15^{\rm h}02^{\rm m}51\overset{\rm s}{.}7$, decl. (J2000) $= -41^\circ56'33''$ (Reynolds & Gilmore 1986; Winkler & Long 1997) so that the zero for the photoelectron direction is aligned with a circularly symmetric polarization model at the position of the event. If the PA in SN 1006 northeast has a circular symmetry rather than a uniform distribution, we will find a significantly larger PD due to less depolarization. Using the aligned events files, region "Shell" has $\mathrm{PD_{align}} = 21.9\% \pm 3.5\%$ at a significance of 6.2σ, similar to that obtained from the uniform PA model ($\mathrm{PD} = 22.4\% \pm 3.5\%$; see Table 1).[57] This means that we cannot distinguish the radial and uniform magnetic orientation models based on current IXPE observations, which only covered the northeastern X-ray-bright limb of SN 1006. The obtained $\mathrm{PA_{align}} = 0\overset{\circ}{.}9 \pm 4\overset{\circ}{.}6$ strongly favors the radial magnetic field ($\mathrm{PA_{align}} = 0^\circ$) over a tangential magnetic morphology ($\mathrm{PA_{align}} = 90^\circ$).

3.3. Spectropolarimetric Analysis of Regions

A different approach to calculate the polarization of the five regions is to use the *I*, *Q*, and *U* spectra. We extracted source spectra from regions "Shell" and A–D and background spectra from "bkg 2022" for the 2022 observation and "bkg 2023" for

[57] Similar results are obtained by taking the SNR center ($15^{\rm h}02^{\rm m}54\overset{\rm s}{.}9$, $-41^\circ56'8\overset{''}{.}0$, J2000) measured by Katsuda et al. (2009): $\mathrm{PD_{align}} = 21.8 \pm 3.5\%$, $\mathrm{PA_{align}} = 1\overset{\circ}{.}5 \pm 4\overset{\circ}{.}6$.

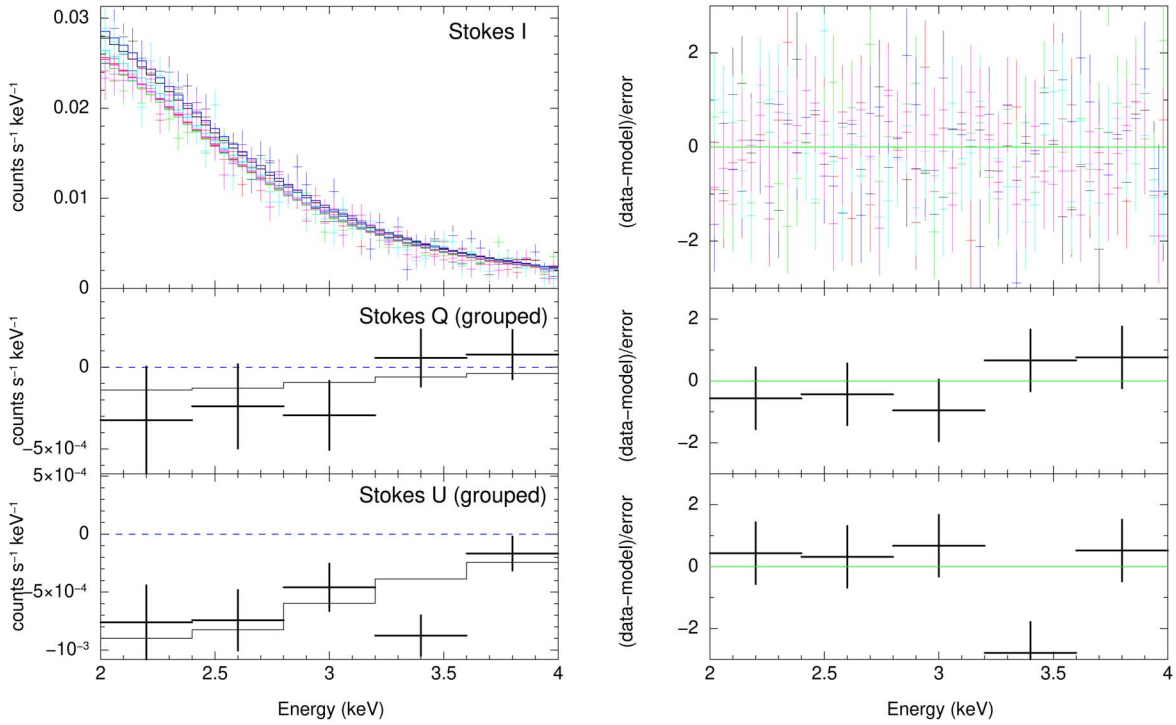

Figure 4. Left: Stokes I, Q, and U spectra of the region "Shell" (data points) and the best-fit model (solid lines). Right: residuals in terms of (data−model)/error. The six Stokes I spectra from two observations are coded using different colors. The six Stokes Q and U spectra are grouped for better visualization.

Table 1
Polarization Results of Five Regions by IXPE and Radio Observations

Region	IXPE (Polarimetric)			IXPE (Spectropolarimetric)			Radio	
	PD (%)	PA (deg)	σ	PD (%)	PA (deg)	Γ	PD_r (%)	PA_r (deg)
Shell	22.4 ± 3.5	-45.4 ± 4.5	6.3	20.2 ± 3.3	-49.4 ± 4.7	2.77 ± 0.04	14.5 ± 0.2	-36.3 ± 0.4
A	20.7 ± 4.5	-49.5 ± 6.2	4.6	21.3 ± 4.7	-56.1 ± 6.2	2.77 ± 0.05	12.5 ± 0.5	-58.4 ± 1.0
B	22.8 ± 4.9	-43.7 ± 6.2	4.6	18.5 ± 4.8	-44.8 ± 7.5	2.65 ± 0.06	19.1 ± 0.6	-28.2 ± 0.9
C	21.9 ± 6.4	-40.0 ± 8.3	3.4	27.5 ± 6.6	-45.3 ± 6.5	2.82 ± 0.07	18.2 ± 0.4	-28.0 ± 0.7
D	<38.8	Undetermined	2.5	<31.8	Undetermined	3.11 ± 0.09	13.9 ± 0.4	-39.8 ± 0.8

Note. The regions are denoted in Figure 3. The polarization results are obtained using the 2–4 keV data, and the errors are provided at the 1σ confidence level. The photon indexes Γ are 2.74 ± 0.01, 2.72 ± 0.01, 2.68 ± 0.01, 2.87 ± 0.01, and 3.05 ± 0.02 for the five regions by fitting the XMM-Newton spectra in 0.8–8 keV. The angle of polarization in the radio band PA_r is calculated using a uniform RM of 12 rad m^{-2} (Reynoso et al. 2013).

the 2023 observations (see regions in Figure 3). For each region, we jointly fit the background-subtracted I, Q, and U spectra with a model combining foreground absorption, a power-law spectrum, and a PD and PA constant over the 2–4 keV energy band (*tbabs* ∗ *powerlaw* ∗ *constpol* in XSpec). Since the foreground absorption can hardly be constrained with the >2 keV photons, we needed to calculate $N_{\rm H}$ by fitting the XMM-Newton spectra using the *tbabs* ∗ *powerlaw* model. The XMM-Newton spectral fit gives the foreground gas column density $N_{\rm H} = 1.93(\pm 0.03) \times 10^{21}$ cm^{-2} for the shell region. Then we fixed $N_{\rm H}$ in the IXPE spectropolarimetric analysis.

Figure 4 shows the I, Q, and U spectra of region "Shell," the best-fit model, and the residuals. The spectral fits produced good fit statistics with $\chi^2/{\rm dof} = 335.63/349 = 0.96$ for the "Shell" region and $\chi^2/{\rm dof} = 0.98$–1.18 for regions A–D. The best-fit PD, PA, and photon index Γ in each region are shown in Table 1. The polarization parameters obtained from the spectropolarimetric analysis agree with the polarimetric results (using the PCUBE algorithm in *xpbin*). Moreover, in the "Shell" region, the photon index $\Gamma = 2.77 \pm 0.04$ of the IXPE spectra is consistent with that given by the XMM-Newton spectral fit $\Gamma = 2.74 \pm 0.01$. The consistency is also found for smaller-scale regions.

4. Discussion

4.1. Magnetic Orientation

The IXPE observations reveal the magnetic field aligned with the shock normal in the northeastern shell of SN 1006 (see Section 3.2). The measured magnetic position angle of $44\overset{\circ}{.}6 \pm 4\overset{\circ}{.}5$ is compatible with the position angle of 24°—58° of the region "Shell" with respect to the SNR center (position angle = 90° for the east of SN 1006 and 0° for the north). This is also consistent with a radial magnetic field configuration in the observed region.

The origin of radial magnetic orientation in young SNRs is still not fully understood, but a few explanations have been proposed (see detailed discussions in Vink et al. 2022b). One

explanation invokes MHD instabilities introduced by density fluctuation. Young SNRs in an inhomogeneous ambient medium drive Richtmyer–Meshkov instabilities (RMIs), which lead to amplifying the radial component of the magnetic fields (Giacalone & Jokipii 2007; Inoue et al. 2013). This scenario requires density fluctuations in the ambient medium, which could be valid for remnants in a cloudy medium. However, SN 1006 evolves in a fairly uniform, tenuous medium 560 pc above the Galactic plane (Acero et al. 2007; Giuffrida et al. 2022). It lacks observational evidence of a large density fluctuation in the northeast for driving strong magnetic turbulence.

An alternative explanation of the radial magnetic fields in the northeastern shell of SN 1006 is related to efficient particle acceleration (West et al. 2017). If the CRs are more efficiently accelerated when the magnetic fields are quasi-parallel to the shock normal, the CR electron density will be amplified in the radial magnetic fields and suppressed in the tangential fields. In this case, even if the magnetic orientation is totally random, the X-ray synchrotron emission will tend to probe the enhanced CR electrons that align the radial magnetic field, resulting in an apparent radial magnetic distribution. However, as simulated by West et al. (2017), purely random magnetic fields would predict a spherically symmetric rim, which does not explain the limb-brightened morphology of SN 1006 (see Figure 1). Moreover, a problem with this explanation for the radial magnetic field orientation in the X-ray regime is that the 10–100 TeV electrons emitting X-rays have diffused away from the region from which they originated. How much of an effect that has depends on the length scales of the regions with radial magnetic field orientations compared to the diffusion length scale (see Vink et al. 2022b).

It is likely that the preexisting magnetic fields of SN 1006 consist of a northeast–southwest orientated component, which it kept, to some extent, after shock propagation (Reynoso et al. 2013). Our IXPE observations did not cover the whole SNR to test this hypothesis, but this was supported by the radio polarization measurement of the southeastern and northwestern portions of the shells in SN 1006 (Reynoso et al. 2013). This northeast–southwest magnetic distribution is favored by 3D MHD simulations, which found that the quasi-parallel CR acceleration model best reproduces the radio morphology (Bocchino et al. 2011) and polarization images of SN 1006 (Schneiter et al. 2015).

The X-ray PA distribution of SN 1006 is consistent with efficient quasi-parallel CR acceleration, which enhances the CR electron density and thus the synchrotron emission in the northeastern and southwestern limbs of SN 1006. Moreover, turbulent magnetic fields can be generated in the quasi-parallel case and vanish in the quasi-perpendicular case (Caprioli & Spitkovsky 2014). This can explain the PD $<$ $\mathrm{PD_{max}}$ in the northeastern shell of SN 1006.

4.2. Magnetic Turbulence

The X-ray PD of the northeastern shell of SN 1006 ($\mathrm{PD} = 22.4\% \pm 3.5\%$) is smaller than the theoretical maximum value of $\mathrm{PD_{max}} = 80\%$ for a photon index of $\Gamma = 2.74$, supporting that the magnetic fields are turbulent.

The turbulent magnetic fields in the upstream can be generated by streaming instabilities driven by the CR precursors (Bell 2004). The length scale of the nonresonant Bell instability for the most rapid growth mode is given as (Bell 2004)

$$l_{\rm Bell} \sim 2 \times 10^{17}\ {\rm cm} \left(\frac{V_{\rm s}}{5\times10^{3}\ {\rm km\ s^{-1}}}\right)^{-3} \left(\frac{n_0}{0.05\ {\rm cm^{-3}}}\right)^{-1} \left(\frac{E_{\rm max}}{100\ {\rm TeV}}\right) \left(\frac{B_0}{3\ \mu{\rm G}}\right), \quad (1)$$

where we take the shock velocity $V_{\rm s} \sim 5\times10^{3}\ {\rm km\ s^{-1}}$ (Katsuda et al. 2009), ambient density $n_0 \sim 0.05\ {\rm cm^{-3}}$ (Acero et al. 2007), and maximum energy $E_{\rm max} \sim 100$ TeV (Acero et al. 2010).

Assuming that the magnetic turbulence in the postshock has similar properties to that in the preshock, we can compare the maximum length scale of the Bell instability with the spatial resolution of IXPE, $l_{\rm IXPE}$. One expects to observe some highly polarized structures when $l_{\rm Bell} > \min(l_{\rm X}, l_{\rm IXPE})$, where $l_{\rm X}$ is the synchrotron rim width, and $l_{\rm IXPE}$ is the structure size observed with IXPE. The FWHM rim width in the 2–7 keV band is 5″–48″ (Ressler et al. 2014), with an average value of 25″ (8×10^{17} cm) for the outer rim and 15″ (5×10^{17} cm) for the inner rim. The angular resolution of IXPE is ∼30″, corresponding to 10^{18} cm for SN 1006, but the regions we selected are a few arcminutes in size. Therefore, the magnetic turbulence scale is smaller than the typical rim width and cannot be resolved with IXPE, which could explain the relatively low PD. We caution that the Bell instability is predicted for the preshock region, while magnetic turbulence properties in the postshock are unclear. Moreover, it is unclear whether the Bell instability can result in radially distributed magnetic fields observed with IXPE. In a more realistic case, the PD distribution depends not only on the telescope resolution or rim width but also on the initial turbulence models and nonlinear physics of turbulent cascades (Bykov et al. 2020).

The Bell mechanism is not the only process to drive turbulent magnetic fields. Shock interaction with the inhomogeneous medium can lead to magnetic amplification and turbulence in both preshock and postshock regions via a turbulent dynamo (Giacalone & Jokipii 2007; Beresnyak et al. 2009; Drury & Downes 2012; Inoue et al. 2013; Xu & Lazarian 2017). The characteristic scale of the turbulent modification of the magnetic field $l_{\rm RMI}$ depends on the density fluctuation scale $l_{\Delta\rho}$ as (Inoue et al. 2013) $l_{\rm RMI} \sim l_{\Delta\rho}/(r_c A)$, where r_c is the shock compression ratio, $\Delta\rho$ is the density fluctuation, and $A \simeq (\Delta\rho/\rho)(1+\Delta\rho/\rho)$. This scale could be large in SN 1006 compared to $l_{\rm Bell}$, since the remnant evolves in a fairly uniform interstellar medium in the northeast and south (Giuffrida et al. 2022). The northeastern shell of SN 1006 has a very low density of 0.05–0.085 $\mathrm{cm^{-3}}$ (Acero et al. 2007; Katsuda et al. 2009), although there is evidence for denser gas in the northwest with enhanced H_α and far-UV emission (e.g., Winkler et al. 2003; Korreck et al. 2004). The X-ray proper-motion measurements found that the northeastern shell across different azimuthal angles expands at nearly constant velocities (Katsuda et al. 2009), which requires a homogeneous ambient medium beyond the shell.

Due to the small density fluctuation, it is likely that the turbulent dynamo is less efficient in SN 1006 than in young SNRs in the clumpy medium. We suggest that CR-induced instabilities could set the magnetic turbulence in SN 1006.

Table 2
X-Ray PD, Shock Velocity, and Ambient Density n_0 of Cas A, Tycho, and SN 1006 Northeast

	PD (Rim) (%)	PD (SNR) (%)	PD (Peak) (%)	V_s (km s^{-1})	n_0 (cm^{-3})	References
Cas A	4.5 ± 1.0	2.5 ± 0.5	~15	~5800	0.9 ± 0.3	[1], [2], [3]
Tycho	12 ± 2	9 ± 2	23 ± 4	~4600	~0.1–0.2	[4], [5], [6]
SN 1006 NE	22.4 ± 3.5	⋯	31 ± 8	~5000	~0.05–0.085	[7], [8], [9], [10]

Note. The PD values are taken from the nonthermal component. References: [1] Vink et al. (2022b), [2] Vink et al. (2022a), [3] Lee et al. (2014), [4] Ferrazzoli et al. (2023), [5] Hughes (2000), [6] Williams et al. (2013), [7] this paper, [8] Acero et al. (2007), [9] Katsuda et al. (2009), [10] Giuffrida et al. (2022).

4.3. Comparison between SNRs Observed with IXPE

To date, we have X-ray polarization measurements for three young SNRs: Cas A, Tycho, and SN 1006. IXPE has already revealed some interesting differences and similarities among them.

A remarkable similarity is the presence of predominantly radial magnetic fields at the immediate postshock. In contrast, old SNRs show tangential magnetic field orientation (Gao et al. 2011), which is believed to originate from compressing the tangential components of ambient magnetic fields. This reinforces that the magnetic fields in young SNRs probed by X-ray polarimetry are not generated by compressing but need other mechanisms to work. As discussed in Section 4.1, these mechanisms invoke MHD instabilities and efficient CR acceleration that are crucial for understanding CR acceleration mechanisms in SNRs. But these three SNRs do not necessarily share the origin of their radial magnetic morphology, since one mechanism may dominate over others in specific cases. Compared to Cas A and Tycho (Vink et al. 2022b; Ferrazzoli et al. 2023), the radial magnetic morphology of SN 1006 northeast likely favors the efficient quasi-parallel CR acceleration in the preexisting field over the MHD instabilities from density fluctuations.

The three young SNRs show significant differences in the degree of polarization, as listed in Table 2. At the forward shock, the X-ray PD in SN 1006 is around twice that in Tycho ($12\% \pm 2\%$; Ferrazzoli et al. 2023) and five times that in Cas A ($4.5\% \pm 1.0\%$; Vink et al. (2022b); see Table 2). This comparison hints that the three young SNRs do not have the same level of turbulent magnetic fields in the immediate postshock region.

Bandiera & Petruk (2016) provided analytic formulae for calculating the polarization parameters of SNRs in turbulent magnetic fields. Under a simplifying assumption that the magnetic field is a combination of an ordered component $\bar{B}$ and a random component with isotropic Gaussian distribution (with a kernel of σ_B), the PD is a function of the turbulence level $\sigma_B/\bar{B}$ and the photon index Γ (see their Equation (31)). For the "Shell" region of SN 1006 with a photon index $\Gamma = 2.74$, we obtain $\sigma_B/\bar{B} = 1.2^{+0.2}_{-0.1}$. We also derived $\sigma_B/\bar{B} \approx 1.8$ in the Tycho rim with $\Gamma = 2.82$ and $\sigma_B/\bar{B} \approx 3.3$ for Cas A in its outer rim with $\Gamma = 3.0$. The comparison shows that the ratio between random and ordered magnetic fields is largest in Cas A and smallest in SN 1006. Note that the $\sigma_B/\bar{B}$ values obtained above are based on a simplified assumption of the magnetic field decomposition. They have a different meaning in physics from the magnetic amplification ratio of 10–100 (between the actual field strength in the downstream and ambient field strength) derived from the profiles of the nonthermal X-ray filaments (Vink & Laming 2003).

What causes the different turbulence levels among the young SNRs needs more investigation, but a possible cause is the different environments. As discussed in Section 4.2, SN 1006 is a peculiar case with a tenuous and smooth ambient medium, so the magnetic turbulence is likely generated purely by CR-induced instability. Cas A is a young core-collapse SNR evolving in its highly clumpy progenitor winds (Vink et al. 1996; Chevalier & Oishi 2003; Koo et al. 2023). The diffuse part of the circumstellar medium has an average density of $0.9 \pm 0.3\,\mathrm{cm}^{-3}$, while the dense winds contain many knotty structures a few orders of magnitude denser than the diffuse gas (Peimbert & van den Bergh 1971; Hwang & Laming 2009; Lee et al. 2014; Koo et al. 2023). Due to the large density fluctuation, the length scale of the turbulence-modified magnetic fields l_{RMI} should be small, and the turbulent dynamo can play an important role in Cas A. Tycho has a Type Ia origin, and the average ambient density is 0.1–0.2 cm^{-3} (e.g., Williams et al. 2013). Nevertheless, the surrounding medium of Tycho is not uniform. The radio and X-ray proper-motion observations of Tycho have revealed that the SNR is experiencing strong deceleration in the northeast and east (Reynoso et al. 1997; Williams et al. 2016; Tanaka et al. 2021). The deceleration is suggested to result from a very recent interaction of the SNR with a surrounding molecular bubble swept up by the progenitor winds (Lee et al. 2004; Zhou et al. 2016). Therefore, the density fluctuation can cause some magnetic turbulence in Tycho.

Given the aforementioned environmental properties of Cas A, Tycho, and SN 1006, the MHD turbulent dynamo can work at a decreasing level for these remnants. This might explain the decreasing magnetic turbulence and thus increasing PD in the three SNRs, although we do not exclude the possibilities that other mechanisms might also play a part and CR-induced instability alone might cause different PDs. Our IXPE observations suggest that magnetic turbulence and, ultimately, CR acceleration in SNRs is environment-dependent (Xu & Lazarian 2022).

4.4. Comparison between the X-Ray and Radio Polarization

The IXPE observation of SN 1006 reveals a possible difference with the radio polarization (Reynoso et al. 2013).

As shown in Table 1, the average angle of polarization in the radio band is $\mathrm{PA}_r = -36\overset{\circ}{.}3 \pm 0\overset{\circ}{.}4$, while the X-ray value is $\mathrm{PA} = -45\overset{\circ}{.}4 \pm 4\overset{\circ}{.}5$. We caution that a uniform RM $= 12\,\mathrm{rad\,m}^{-2}$ is used to correct the Faraday rotation, and the error of the RM is not included. Due to the large uncertainty of the RM value (Reynoso et al. 2013) and its influence on PA_r, we cannot conclude that there is a large discrepancy in PA between the radio and X-ray bands.

The X-ray PD ($22.4\% \pm 3.5\%$) in the SNR shell is larger than the radio value ($14.5\% \pm 0.2\%$) at an $\sim 2\sigma$ significance

level. Although the significance is not sufficiently large, a discrepancy in PD between X-ray and radio measurements is not unexpected. First, the intrinsic PD of the X-rays can be larger than that of the radio emission. The maximum polarization PD $_{\max} = \Gamma/(\Gamma + 2/3)$ is 80% in the X-ray band with $\Gamma = 2.74$ and 70.5% in the radio band with $\Gamma = 1.6$ (Reynoso et al. 2013). Second, the X-ray emission is radiated from a smaller layer than the radio emission and thus may have less depolarization. The synchrotron emissivity profile reflects the strength of the magnetic fields and particle distribution. The X-ray synchrotron emission originates from electrons freshly accelerated to TeV energy, which lose their energy E quickly with a characteristic timescale of $\tau_{\rm loss} = 640/(B^2E)$ s, where the electron energy, E, is in units of erg, and the magnetic field strength, B, is in units of gauss (e.g., Reynolds 1998). Radiative energy losses as particles advect downstream can shrink the rim width in the higher energy band, $l_{\rm loss} \approx v_d\tau_{\rm loss}$, where v_d is the fluid velocity downstream of the shock. The rim width might also be regulated by the diffusion transport of particles and/or magnetic damping, but Ressler et al. (2014) compared with the observations and supported that the filament widths in SN 1006 decrease with increasing photon frequency ν (width $\propto\nu^{m_E}$, $m_E \sim -0.3$ to -0.8). With a larger emitting volume than the X-rays, the radio emission also tends to be depolarized as the PAs vary along the line of sight. Third, if the RM is nonuniform, but we incorrectly used a uniform RM, the calculated PA$_r$ value may vary across the shell. Consequently, combining the radio polarization data from a large region might cause a depolarization.

5. Summary

In this paper, we report the first X-ray polarization imaging observations of the northeastern shell of SN 1006. The main results are summarized as follows.

1. We show the spatial distribution of the PD and PA of the shell. The PA in different pixels shows a tangential distribution along the shell, suggesting that the overall magnetic orientation parallels the shock normal or has a radial distribution.
2. The overall degree of polarization in the northeastern shell is $22.4\% \pm 35\%$ and PA $= -45\overset{\circ}{.}5 \pm 4\overset{\circ}{.}5$ (background removed). We checked the variation of the polarization properties by separating the shell into a few regions but did not find significant differences of PD and PA across the shell.
3. The magnetic field orientation in SN 1006 supports the efficient quasi-parallel CR acceleration.
4. We compared X-ray polarization measurements of Cas A, Tycho, and SN 1006. The remarkable similarity is the radially distributed magnetic fields. But they also show an increasing PD, likely reflecting a decreased turbulent level of the magnetic fields. We compared their environmental density and interpreted that the different density and density fluctuations could cause the PD discrepancy between the three SNRs. The IXPE observations thus support that magnetic turbulence is environment-dependent.
5. The X-ray PD in the shell is larger than the radio PD ($14.5\% \pm 0.2\%$) at an $\sim 2\sigma$ level. The possible explanation includes a larger intrinsic PD in X-rays, a larger radio emission emitting area that causes a depolarization, or a depolarization due to applying incorrect RM distribution.

Acknowledgments

The Imaging X-ray Polarimetry Explorer (IXPE) is a joint US and Italian mission. The US contribution is supported by the National Aeronautics and Space Administration (NASA) and led and managed by its Marshall Space Flight Center (MSFC), with industry partner Ball Aerospace (contract NNM15AA18C). The Italian contribution is supported by the Italian Space Agency (Agenzia Spaziale Italiana, ASI) through contract ASI-OHBI-2017-12-I.0, agreements ASI-INAF-2017-12-H0 and ASI-INFN-2017.13-H0, and its Space Science Data Center (SSDC) and by the Istituto Nazionale di Astrofisica (INAF) and the Istituto Nazionale di Fisica Nucleare (INFN) in Italy. This research used data products provided by the IXPE Team (MSFC, SSDC, INAF, and INFN) and distributed with additional software tools by the High-Energy Astrophysics Science Archive Research Center (HEASARC) at NASA Goddard Space Flight Center (GSFC). P.Z. acknowledges the support from NSFC grant No. 12273010 and Nederlandse Organisatie voor Wetenschappelijk Onderzoek (NWO) Veni Fellowship grant No. 639.041.647. C.-Y.N. and Y.J.Y. are supported by a GRF grant of the Hong Kong Government under HKU 17305419. N.B. was supported by the INAF MiniGrant "PWNnumpol—Numerical Studies of Pulsar Wind Nebulae in the Light of IXPE."

Software: ixpeobssim (vers. 30.0; Baldini et al. 2022), DS9 (Joye & Mandel 2003; Smithsonian Astrophysical Observatory 2000), SAS (SAS Development Team 2014), Xspec (vers. 12.9.0u; Arnaud 1996).

Appendix

Figure 5 shows the IXPE DU1 spectrum of the region "Shell," with the background spectrum subtracted. The solid line shows the modeled background spectrum. Above ~4 keV, the background flux becomes comparable to or brighter than the source flux. Therefore, we select only the 2–4 keV energy band to examine the polarization properties.

To investigate whether the polarization parameters vary with the X-ray surface brightness, we calculated the background-

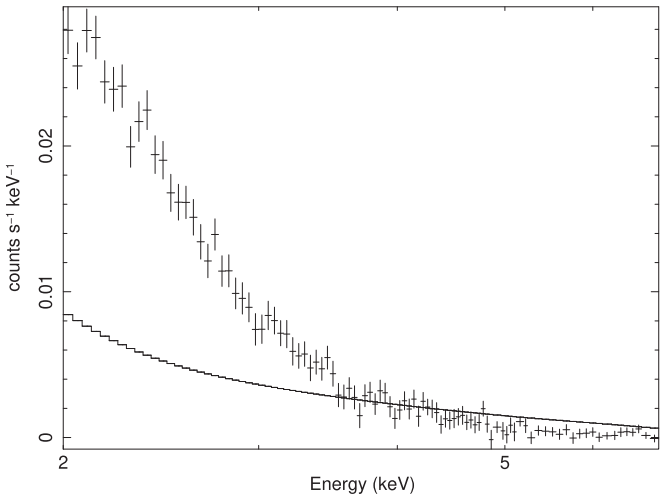

Figure 5. Background-subtracted Stokes I spectrum from DU1 (data points) of the region "Shell" and the background level (solid line).

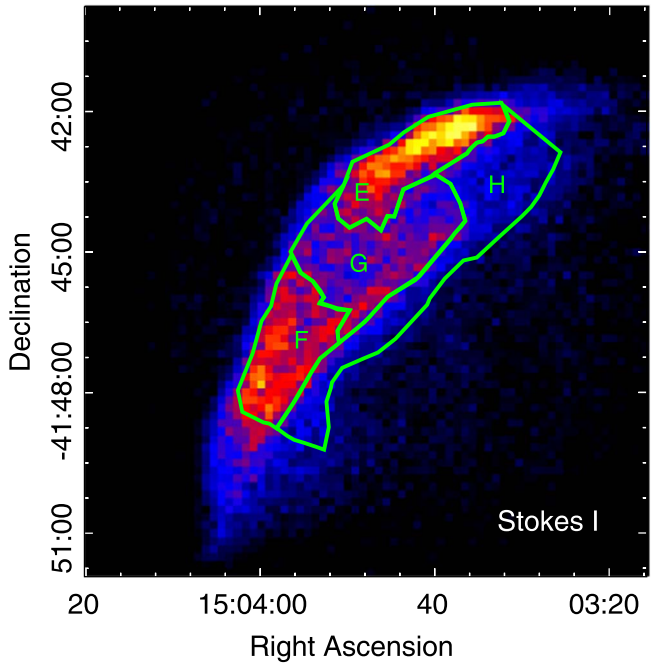

Figure 6. Stokes *I* image overlaid with regions E–H with decreasing brightness.

Table 3
X-Ray Polarization Results of Four Regions with Different X-Ray Brightness

Region	PD (%)	PA (deg)	σ
E	20.5 ± 5.0	-47.1 ± 6.9	4.1
F	22.5 ± 5.4	-36.2 ± 6.9	4.2
G	21.7 ± 5.6	-45.6 ± 7.4	3.9
H	26.0 ± 7.7	-39.0 ± 8.4	3.4

Note. The regions are denoted in Figure 6. The polarization errors are provided at the 1σ confidence level.

subtracted PD and PA in four new regions, E, F, G, and H, with decreasing X-ray brightness (see Figure 6). The obtained results are shown in Table 3. The PD and PA values of the four regions are consistent with each other, suggesting that the PD is near uniform across the shell and independent of the X-ray surface brightness.

ORCID iDs

Ping Zhou https://orcid.org/0000-0002-5683-822X
Dmitry Prokhorov https://orcid.org/0000-0001-6511-4330
Riccardo Ferrazzoli https://orcid.org/0000-0003-1074-8605
Yi-Jung Yang https://orcid.org/0000-0001-9108-573X
Patrick Slane https://orcid.org/0000-0002-6986-6756
Jacco Vink https://orcid.org/0000-0002-4708-4219
Stefano Silvestri https://orcid.org/0000-0002-8665-0105
Niccolò Bucciantini https://orcid.org/0000-0002-8848-1392
Paolo Soffitta https://orcid.org/0000-0002-7781-4104
Doug Swartz https://orcid.org/0000-0002-2954-4461
Philip Kaaret https://orcid.org/0000-0002-3638-0637
Luca Baldini https://orcid.org/0000-0002-9785-7726
Enrico Costa https://orcid.org/0000-0003-4925-8523
C.-Y. Ng https://orcid.org/0000-0002-5847-2612
Dawoon E. Kim https://orcid.org/0000-0001-5717-3736
Victor Doroshenko https://orcid.org/0000-0001-8162-1105
Steven R. Ehlert https://orcid.org/0000-0003-4420-2838
Jeremy Heyl https://orcid.org/0000-0001-9739-367X
Frédéric Marin https://orcid.org/0000-0003-4952-0835
Tsunefumi Mizuno https://orcid.org/0000-0001-7263-0296
Melissa Pesce-Rollins https://orcid.org/0000-0003-1790-8018
Carmelo Sgrò https://orcid.org/0000-0001-5676-6214
Toru Tamagawa https://orcid.org/0000-0002-8801-6263
Martin C. Weisskopf https://orcid.org/0000-0002-5270-4240
Fei Xie https://orcid.org/0000-0002-0105-5826
Iván Agudo https://orcid.org/0000-0002-3777-6182
Lucio A. Antonelli https://orcid.org/0000-0002-5037-9034
Matteo Bachetti https://orcid.org/0000-0002-4576-9337
Wayne H. Baumgartner https://orcid.org/0000-0002-5106-0463
Ronaldo Bellazzini https://orcid.org/0000-0002-2469-7063
Stefano Bianchi https://orcid.org/0000-0002-4622-4240
Stephen D. Bongiorno https://orcid.org/0000-0002-0901-2097
Raffaella Bonino https://orcid.org/0000-0002-4264-1215
Alessandro Brez https://orcid.org/0000-0002-9460-1821
Fiamma Capitanio https://orcid.org/0000-0002-6384-3027
Simone Castellano https://orcid.org/0000-0003-1111-4292
Chien-Ting Chen https://orcid.org/0000-0002-4945-5079
Stefano Ciprini https://orcid.org/0000-0002-0712-2479
Alessandra De Rosa https://orcid.org/0000-0001-5668-6863
Ettore Del Monte https://orcid.org/0000-0002-3013-6334
Laura Di Gesu https://orcid.org/0000-0002-5614-5028
Niccolò Di Lalla https://orcid.org/0000-0002-7574-1298
Alessandro Di Marco https://orcid.org/0000-0003-0331-3259
Immacolata Donnarumma https://orcid.org/0000-0002-4700-4549
Michal Dovčiak https://orcid.org/0000-0003-0079-1239
Teruaki Enoto https://orcid.org/0000-0003-1244-3100
Yuri Evangelista https://orcid.org/0000-0001-6096-6710
Sergio Fabiani https://orcid.org/0000-0003-1533-0283
Javier A. Garcia https://orcid.org/0000-0003-3828-2448
Shuichi Gunji https://orcid.org/0000-0002-5881-2445
Wataru Iwakiri https://orcid.org/0000-0002-0207-9010
Svetlana G. Jorstad https://orcid.org/0000-0001-6158-1708
Fabian Kislat https://orcid.org/0000-0001-7477-0380
Vladimir Karas https://orcid.org/0000-0002-5760-0459
Jeffery J. Kolodziejczak https://orcid.org/0000-0002-0110-6136
Henric Krawczynski https://orcid.org/0000-0002-1084-6507
Fabio La Monaca https://orcid.org/0000-0001-8916-4156
Luca Latronico https://orcid.org/0000-0002-0984-1856
Ioannis Liodakis https://orcid.org/0000-0001-9200-4006
Simone Maldera https://orcid.org/0000-0002-0698-4421
Alberto Manfreda https://orcid.org/0000-0002-0998-4953
Andrea Marinucci https://orcid.org/0000-0002-2055-4946
Alan P. Marscher https://orcid.org/0000-0001-7396-3332
Herman L. Marshall https://orcid.org/0000-0002-6492-1293
Giorgio Matt https://orcid.org/0000-0002-2152-0916
Fabio Muleri https://orcid.org/0000-0003-3331-3794

Michela Negro https://orcid.org/0000-0002-6548-5622
Stephen L. O'Dell https://orcid.org/0000-0002-1868-8056
Nicola Omodei https://orcid.org/0000-0002-5448-7577
Chiara Oppedisano https://orcid.org/0000-0001-6194-4601
Alessandro Papitto https://orcid.org/0000-0001-6289-7413
George G. Pavlov https://orcid.org/0000-0002-7481-5259
Abel L. Peirson https://orcid.org/0000-0001-6292-1911
Matteo Perri https://orcid.org/0000-0003-3613-4409
Pierre-Olivier Petrucci https://orcid.org/0000-0001-6061-3480
Maura Pilia https://orcid.org/0000-0001-7397-8091
Andrea Possenti https://orcid.org/0000-0001-5902-3731
Juri Poutanen https://orcid.org/0000-0002-0983-0049
Simonetta Puccetti https://orcid.org/0000-0002-2734-7835
Brian D. Ramsey https://orcid.org/0000-0003-1548-1524
John Rankin https://orcid.org/0000-0002-9774-0560
Ajay Ratheesh https://orcid.org/0000-0003-0411-4243
Oliver Roberts https://orcid.org/0000-0002-7150-9061
Roger W. Romani https://orcid.org/0000-0001-6711-3286
Gloria Spandre https://orcid.org/0000-0003-0802-3453
Fabrizio Tavecchio https://orcid.org/0000-0003-0256-0995
Roberto Taverna https://orcid.org/0000-0002-1768-618X
Allyn F. Tennant https://orcid.org/0000-0002-9443-6774
Nicholas E. Thomas https://orcid.org/0000-0003-0411-4606
Francesco Tombesi https://orcid.org/0000-0002-6562-8654
Alessio Trois https://orcid.org/0000-0002-3180-6002
Sergey S. Tsygankov https://orcid.org/0000-0002-9679-0793
Roberto Turolla https://orcid.org/0000-0003-3977-8760
Kinwah Wu https://orcid.org/0000-0002-7568-8765
Silvia Zane https://orcid.org/0000-0001-5326-880X

References

Acero, F., Aharonian, F., Akhperjanian, A. G., et al. 2010, A&A, 516, A62
Acero, F., Ballet, J., & Decourchelle, A. 2007, A&A, 475, 883
Arnaud, K. A. 1996, in ASP Conf. Ser. 101, Astronomical Data Analysis Software and Systems V, ed. G. H. Jacoby & J. Barnes (San Francisco, CA: ASP), 17
Baade, W., & Zwicky, F. 1934, PNAS, 20, 259
Baldini, L., Bucciantini, N., Lalla, N. D., et al. 2022, SoftX, 19, 101194
Bamba, A., Yamazaki, R., Ueno, M., & Koyama, K. 2004, AdSpR, 33, 376
Bandiera, R., & Petruk, O. 2016, MNRAS, 459, 178
Bell, A. R. 2004, MNRAS, 353, 550
Bellazzini, R., Angelini, F., Baldini, L., et al. 2006, NIMPA, 560, 425
Beresnyak, A., Jones, T. W., & Lazarian, A. 2009, ApJ, 707, 1541
Bocchino, F., Orlando, S., Miceli, M., & Petruk, O. 2011, A&A, 531, A129
Bykov, A. M., Uvarov, Y. A., Slane, P., & Ellison, D. C. 2020, ApJ, 899, 142
Caprioli, D., & Spitkovsky, A. 2014, ApJ, 783, 91
Chevalier, R. A., & Oishi, J. 2003, ApJL, 593, L23
Condon, B., Lemoine-Goumard, M., Acero, F., & Katagiri, H. 2017, ApJ, 851, 100
Costa, E., Soffitta, P., Bellazzini, R., et al. 2001, Natur, 411, 662
Di Marco, A., Costa, E., Muleri, F., et al. 2022, AJ, 163, 170
Di Marco, A., Soffitta, P., Costa, E., et al. 2023, AJ, 165, 143
Drury, L. O., & Downes, T. P. 2012, MNRAS, 427, 2308
Ferrazzoli, R., Slane, P., Prokhorov, D., et al. 2023, ApJ, 945, 52
Fulbright, M. S., & Reynolds, S. P. 1990, ApJ, 357, 591
Gao, X. Y., Han, J. L., Reich, W., et al. 2011, A&A, 529, A159
Giacalone, J., & Jokipii, J. R. 2007, ApJL, 663, L41
Giuffrida, R., Miceli, M., Caprioli, D., et al. 2022, NatCo, 13, 5098
Hughes, J. P. 2000, ApJL, 545, L53
Hwang, U., & Laming, J. M. 2009, ApJ, 703, 883
Inoue, T., Shimoda, J., Ohira, Y., & Yamazaki, R. 2013, ApJL, 772, L20
Joye, W. A., & Mandel, E. 2003, in ASP Conf. Ser. 295, Astronomical Data Analysis Software and Systems XII, ed. H. E. Payne, R. I. Jedrzejewski, & R. N. Hook (San Francisco, CA: ASP), 489
Katsuda, S., Petre, R., Long, K. S., et al. 2009, ApJL, 692, L105
Koo, B.-C., Kim, D., Yoon, S.-C., & Raymond, J. C. 2023, ApJ, 945, 158
Korreck, K. E., Raymond, J. C., Zurbuchen, T. H., & Ghavamian, P. 2004, ApJ, 615, 280
Koyama, K., et al. 1995, Natur, 378, 255
Lee, J.-J., Koo, B.-C., & Tatematsu, K. 2004, ApJL, 605, L113
Lee, J.-J., Park, S., Hughes, J. P., & Slane, P. O. 2014, ApJ, 789, 7
Li, J.-T., Decourchelle, A., Miceli, M., Vink, J., & Bocchino, F. 2016, MNRAS, 462, 158
Parizot, E., Marcowith, A., Ballet, J., & Gallant, Y. A. 2006, A&A, 453, 387
Peimbert, M., & van den Bergh, S. 1971, ApJ, 167, 223
Petruk, O., Dubner, G., Castelletti, G., et al. 2009, MNRAS, 393, 1034
Ressler, S. M., Katsuda, S., Reynolds, S. P., et al. 2014, ApJ, 790, 85
Reynolds, S. P. 1998, ApJ, 493, 375
Reynolds, S. P., & Gilmore, D. M. 1986, AJ, 92, 1138
Reynoso, E. M., Hughes, J. P., & Moffett, D. A. 2013, AJ, 145, 104
Reynoso, E. M., Moffett, D. A., Goss, W. M., et al. 1997, ApJ, 491, 816
Rothenflug, R., Ballet, J., Dubner, G., et al. 2004, A&A, 425, 121
SAS development team, 2014 SAS: Science Analysis System for XMM-Newton observatory, Astrophysics Source Code Library, ascl:1404.004
Schneiter, E. M., Velázquez, P. F., Reynoso, E. M., Esquivel, A., & De Colle, F. 2015, MNRAS, 449, 88
Smithsonian Astrophysical Observatory, 2000 SAOImage DS9: A Utility for Displaying Astronomical Images in the X11 Window Environment, Astrophysics Source Code Library, ascl:0003.002
Tanaka, T., Okuno, T., Uchida, H., et al. 2021, ApJL, 906, L3
Uchiyama, Y., Aharonian, F. A., Tanaka, T., Takahashi, T., & Maeda, Y. 2007, Natur, 449, 576
van der Laan, H. 1962, MNRAS, 124, 125
Vink, J., Kaastra, J. S., & Bleeker, J. A. M. 1996, A&A, 307, L41
Vink, J., & Laming, J. M. 2003, ApJ, 584, 758
Vink, J., Patnaude, D. J., & Castro, D. 2022a, ApJ, 929, 57
Vink, J., Prokhorov, D., Ferrazzoli, R., et al. 2022b, ApJ, 938, 40
Weisskopf, M. C., Soffitta, P., Baldini, L., et al. 2022, JATIS, 8, 026002
West, J. L., Jaffe, T., Ferrand, G., Safi-Harb, S., & Gaensler, B. M. 2017, ApJL, 849, L22
West, J. L., Safi-Harb, S., Jaffe, T., et al. 2016, A&A, 587, A148
Williams, B. J., Borkowski, K. J., Ghavamian, P., et al. 2013, ApJ, 770, 129
Williams, B. J., Chomiuk, L., Hewitt, J. W., et al. 2016, ApJL, 823, L32
Winkler, P. F., Gupta, G., & Long, K. S. 2003, ApJ, 585, 324
Winkler, P. F., & Long, K. S. 1997, ApJ, 491, 829
Winkler, P. F., Williams, B. J., Reynolds, S. P., et al. 2014, ApJ, 781, 65
Xie, F., Ferrazzoli, R., Soffitta, P., et al. 2021, APh, 128, 102566
Xing, Y., Wang, Z., Zhang, X., & Chen, Y. 2016, ApJ, 823, 44
Xu, S., & Lazarian, A. 2017, ApJ, 850, 126
Xu, S., & Lazarian, A. 2022, ApJ, 925, 48
Zhou, P., Chen, Y., Zhang, Z.-Y., et al. 2016, ApJ, 826, 34